Supporting Information

A fluorescent microporous crystalline dendrimer discriminates vapour molecules

Sae Nakajima, Ken Albrecht, Soh Kushida, Eiji Nishibori, Takashi Kitao, Takashi Uemura, Kimihisa Yamamoto, Uwe H. F. Bunz,* Yohei Yamamoto*

* To whom correspondence should be addressed.
E-mail: uwe.bunz@oci.uni-heidelberg.de, yamamoto@ims.tsukuba.ac.jp

Table of Contents

1. Materials and methods.

Unless otherwise noted, all reagents and solvents were used as received from Aldrich Chemical Co. Ltd, Tokyo Chemical Industry Co. Ltd and Nakarai Tesque Co. The triazine-carbazole dendrimer **1** was synthesized according to the reported procedures.[S1] Photoabsorption and steady-state PL spectra were recorded on a JASCO V-570 spectrophotometer and a JASCO FP-8500 spectrofluorometer, respectively. NMR spectra were recorded on a Bruker AVANCE III 400 (400 MHz) spectrometer by using tetramethylsilane (0 ppm for ^{1}H NMR) as an internal standard. SEM microscopy was performed on a Hitachi model SU-8020 FE-SEM operating at 1 kV. Silicon was used as a substrate. Powder XRD patterns were recorded at 25 °C on a RIGAKU model Miniflex600 diffractometer with a Cu$K\alpha$ radiation source (40 kV and 15 mA), equipped with model D/Tex Ultra2-MF high-speed 1D detector. Powder XRD pattern upon addition of acetonitrile and MeOH were collected on a Rigaku SmartLab Diffractometer, using a Cu anode (λ = 0.154 nm). Synchrotron radiation powder and single crystal XRD was described in the Methods section. Optical and fluorescent microscope observation was carried out using an Olympus model BX53 upright microscope. For the fluorescent microscopy, the excitation light with wavelength λ_{ex} = 340–390 nm was used with the long-pass filter (> 410 nm) for the detection of the images. Differential scanning calorimetry (DSC) traces were measured on a TA Instrument model Q2000 differential scanning calorimeter using unsealed Al sample pans with the sample amount of 5.22 and 4.56 mg for self-assembled fibres and spheres of **1**. Gas uptake studies were performed on a Shimadzu model tristar II 3020 micromeritics automatic surface area and porosimetry analyzer for the N_2 sorption and a MicrotracBEL model BELSORP-max II specific surface area and pore size distribution analyzer for the MeOH and acetonitrile sorption.

2. Self-assembly of 1.

Self-assembly of **1** was conducted by a vapour diffusion method. Typically, a 5 mL vial containing a $CHCl_3$ solution of **1** ($0.05 \leq [\mathbf{1}] \leq 10$ mg mL^{-1}, total amount 2 mL) was placed in a 50 mL vial containing 5 mL of acetonitrile, acetone, or MeOH. The outside vial was capped and then allowed to stand for 3 days at 25 °C. The vapour of the nonsolvent was slowly diffused into the solution, resulting in precipitation over the supersaturated state.

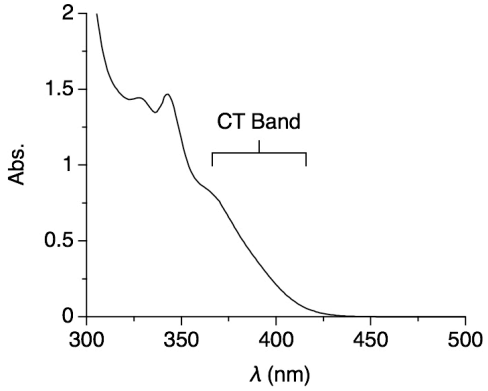

Figure S1. Photoabsorption spectrum of a $CHCl_3$ solution of **1**.

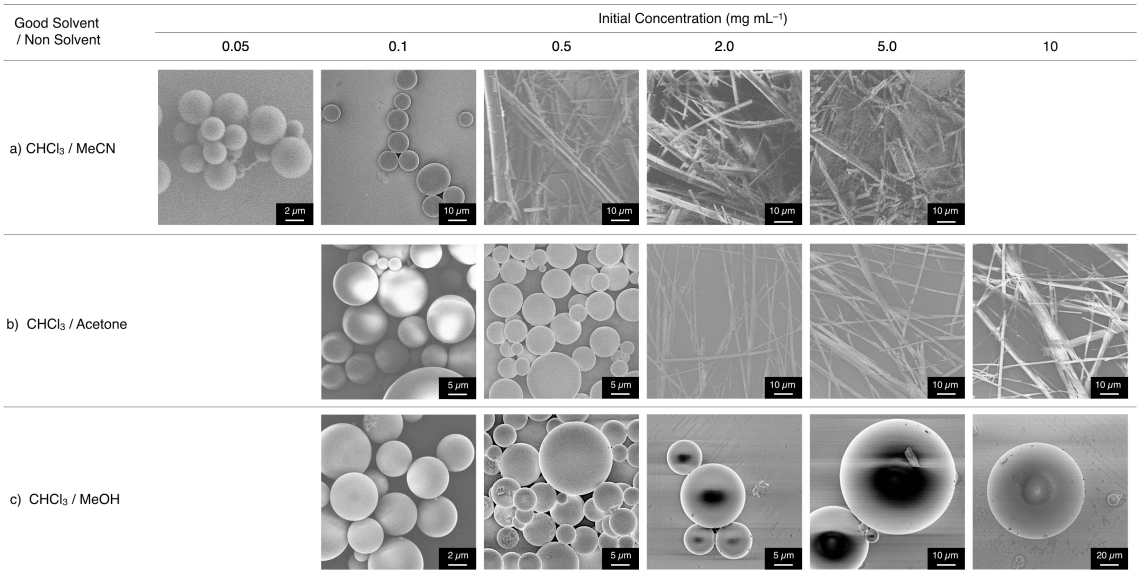

Figure S2. SEM micrographs of self-assembled precipitates of **1** by vapour diffusion of acetonitrile (a), acetone (b), and MeOH (c) into $CHCl_3$ solution of **1** with various initial concentrations.

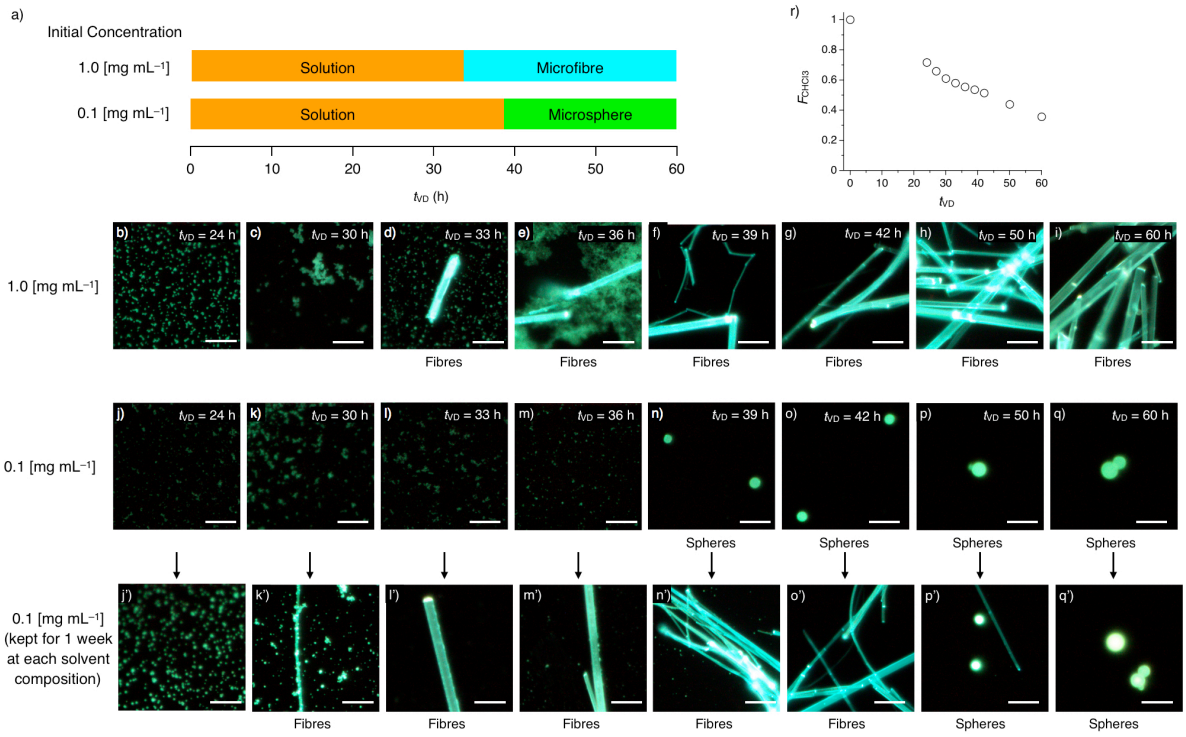

Figure S3. (a) Bar chart of the assembling state of **1** in the vapour diffusion process. t_{VD}: vapour diffusion time. (b–q) Fluorescent micrographs of cast films of solutions or suspensions in the vapour diffusion process of **1** with initial concentration of **1** in $CHCl_3$ of 1.0 mg mL^{-1} (b–i), 0.1 mg mL^{-1} (j–q), and 0.1 mg mL^{-1} that were kept for 1 week at each solvent composition (j'–q'). Scale bars; 10 μm. (r) Plot of F_{CHCl3} versus t_{VD}, determined by ^{1}H-NMR spectroscopy in DMSO-d^6 of the mixed solvent during vapour diffusion. F_{CHCl3}: volume fraction of $CHCl_3$ in $CHCl_3$/MeCN cosolvent.

Dissolution studies of microfibres and microspheres reveal that microfibres are thermodynamically more stable than microspheres. For the experiments, dispersions of microspheres and microfibres were prepared ([**1**] = 2 mg mL^{-1} in MeCN). Then, a 20 μL of the dispersion was poured into a 380 μL of $CHCl_3$/MeCN mixed solvents ([**1**] = 0.1 mg mL^{-1}). The resultant solution or dispersion was centrifuged for 10 min to remove the precipitate, and the supernatant solution was used for photoabsorption measurement. Figure S4a shows plots of I_{abs} (absorbance value at λ = 294 nm, which is normalized by that for F_{CHCl3} = 1) versus F_{CHCl3} for microfibres (blue) and microspheres (green). From the plots, microfibres dissolve at F_{CHCl3} ~0.739, while microspheres dissolve at F_{CHCl3} ~0.588. Then, the Gibbs energy difference from the solution state to the assembling state (ΔG) of **1** is considered by employing the two-state equilibrium model.[S2]

Thus, ΔG from the dissolved **1** to the assembled **1** (ΔG) varies with F_{CHCl3} and is expressed as

$$\Delta G = \Delta G(\text{MeCN}) - m \bullet F_{CHCl3} \quad (1)$$

where ΔG(MeCN) is the Gibbs energy difference between the assembled and disassembled states of **1** in MeCN, and m represents the coefficient of the change of the free energy with the composition of $CHCl_3$.[S2] ΔG is also expressed as

$$\Delta G = -RT \ln K. \quad (2)$$

ΔG = 0 when the ratio of **1** in the solution and assembled state is 1/1, and F_{CHCl3} at this point is defined as F_{CHCl3}(S/A). The equilibrium constant K between the solution and assembly states of **1** is described as

$$K = f_A/f_S = f_A/(1 - f_A) \quad (3)$$

where f_S and f_A represent fractions of **1** in the solution and assembled states, respectively, and, because of the two-state model, $f_S + f_A = 1$. Provided that the macroscopic assemblies are removed from the supernatant solution by centrifugation, f_A is described as

$$f_A = (I_{abs}(S) - I_{abs}) / (I_{abs}(S) - I_{abs}(A))$$
$$= 1 - I_{abs} \quad (4)$$

where I_{abs}(S) (= 1) and I_{abs}(A) (= 0) are the I_{abs} values of the supernatant solutions for the solution and assembled states, respectively. By assigning equation (1)–(4), the resultant curve for I_{abs} versus F_{CHCl3} for microfibres (blue) and microspheres (green) fits well with the experimental plots (Figure S4a, solid curves). The best-fitted parameters of ΔG(MeCN), m, and F_{CHCl3}(S/A) are shown in Table S1.

Figure S4b draws ΔG vs. F_{CHCl3} lines for microfibres (blue) and microspheres (green) using equation (1). From the lines, it is concluded that the microfibres are thermodynamically more stable than microspheres in the whole F_{CHCl3} range. Then, why microspheres were produced in the dilute self-assembly condition? The possible answer is referred to the difference of the precipitation rate: microspheres precipitate much rapid in comparison with microfibres. These conclusions are given by rapid precipitation and aging experiments. Thus, $CHCl_3$ solution of **1** was poured into a $CHCl_3$/MeCN mixed solvent with F_{CHCl3} = 0.50, 0.58, 0.65, and 0.75 ([**1**] = 0.1 mg mL^{-1}). In case that F_{CHCl3} = 0.50 and 0.58, microspheres form as soon as the reprecipitation are processed (Fig. S4c and d). On the other hand, no precipitation takes place for samples with F_{CHCl3} = 0.65 and 0.75 (Fig. S4e and f). However, after the solution or suspension are aged for one week, microfibres are formed in case of F_{CHCl3} = 0.58 and 0.65 (Fig. S4d' and e'). Accordingly, the formation of microfibres are sluggish in comparison with the precipitation of microspheres. Note that, as shown in Fig. S2a, microfibre formation is prior to the formation of microspheres by elevating the initial concentration ([**1**] > 0.5 mg mL^{-1}), indicating that increasing the initial concentration shorten the growth period of the microfibre.

The behaviours of the morphological transformation in the vapour diffusion process (Figure S3j–q → j'–q') are clearly explained using diagram in Figure S4h. In a dilute condition ([**1**] = 0.1 mg mL^{-1}), no precipitation takes place at t_{VD} = 30–36 h (Figure S3k–m). However, by standing the solution while maintaining F_{CHCl3}, microfibres forms after 1 week of aging (Figure S3k'–m'). In case of t_{VD} = 39–42 h, microspheres form (Figure S3n and o). However, the microspheres transform into microfibres after 1 week of aging (Figure S3n' and o'). On the other hand, for t_{VD} = 50–60 h, such sphere-to-fibre morphological transformation are hardly observed (Figure S3p, q → p', q'), possibly because the content of the nonsolvent (MeCN) are high enough to disturb the re-dissolution of **1** in the microsphere assembly.

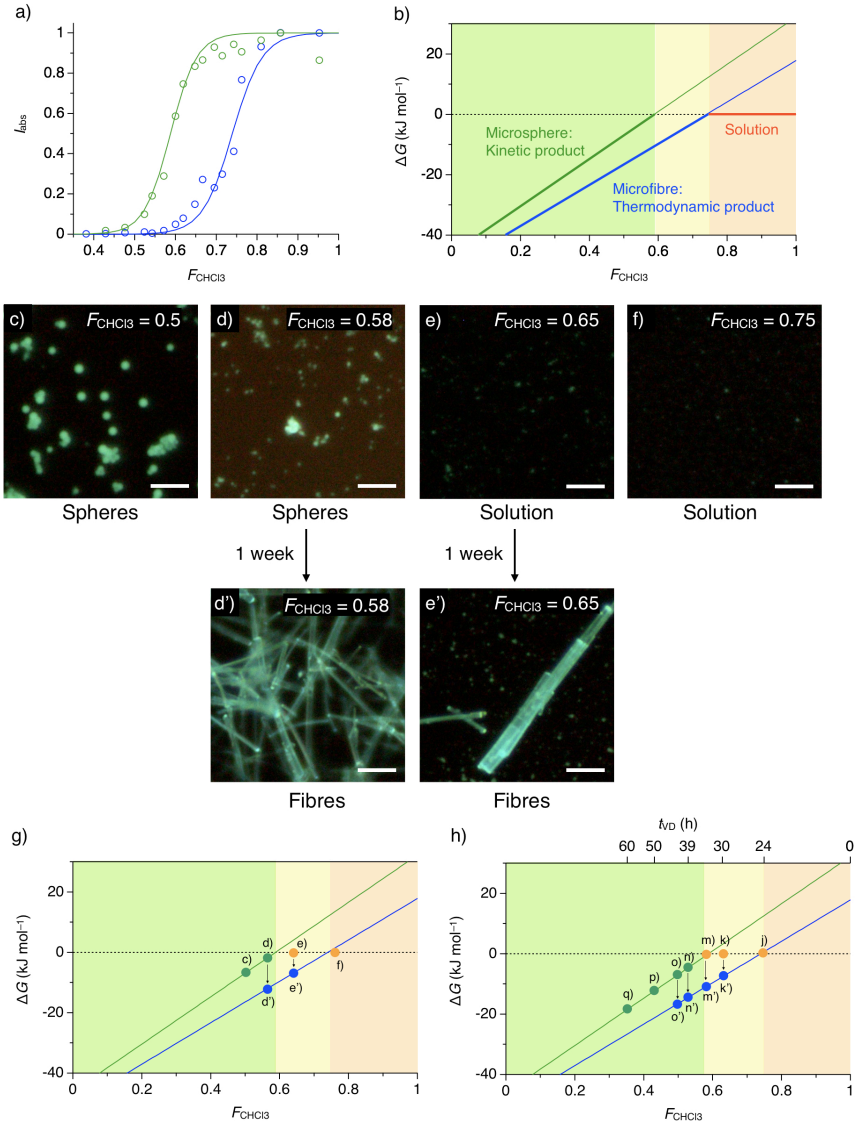

Figure S4. (a) Plots of the normalized absorbance (I_{abs}) at 294 nm of the dissolved **1** from the self-assembled microfibres (blue) and microspheres (green) in the supernatant solution versus volume fraction of $CHCl_3$ (F_{CHCl3}). For experiments, $CHCl_3$ was poured into the MeCN suspension of **1**. The solid curves show fittings using equations (1)–(4). (b) The relation of ΔG versus F_{CHCl3} for microfibres (blue) and microspheres (green) using equation (1) and parameters in Table S1. (c–f) Fluorescent micrographs of cast films of **1**, prepared by a rapid reprecipitation from $CHCl_3$ solution of **1**, which was poured into $CHCl_3$/MeCN cosolvent with F_{CHCl3} = 0.5 (c), 0.58 (d), 0.65 (e), and 0.75 (f), and that with F_{CHCl3} = 0.58 (d') and 0.65 (e') after being aged for 1 week. (g) Plots of each state in Fig. S4 (c)–(f), (d'), and (e'). (h) Plots of each state in Fig. S3(j)–(q) and (k')–(o').

Table S1. Parameters obtained from the fittings of the absorption plots versus F_{CHCl3}.

	ΔG(MeCN) /kJ mol^{-1}	m /kJ mol^{-1}	F_{CHCl3}(S/A)
Microfibre	–50.7	68.6	0.739
Microsphere	–46.0	78.3	0.588

3. XRD measurements and Thermal analysis.

SR single-crystal XRD measurement and analysis.

Synchrotron radiation (SR) XRD data of a single crystal of **1** were collected at 270 K and 200 K. The crystal dimension was 300 × 30 × 15 μm^3. The diffraction data were recorded on a CCD detector at SPring-8 beam line BL02B1 (Hyogo, Japan) (λ = 0.7010 Å). The data were indexed and processed using the RAPID-AUTO program (RIGAKU). The unit cell parameters and data status are listed in Tables S2 and S3. From the low-resolution ($\sin\theta/\lambda < 0.16$ Å^{-1}) single-crystal diffraction data, it was not possible to solve the structure because of the poor crystal quality. Typical diffraction data recorded by the CCD detector are shown in Figure S5. No Bragg reflections were available in the high-angle region, and smeared Bragg peaks due to the low crystal quality were observed in the low-angle region. The candidates of the space group and lattice parameters were uniquely determined from the data.

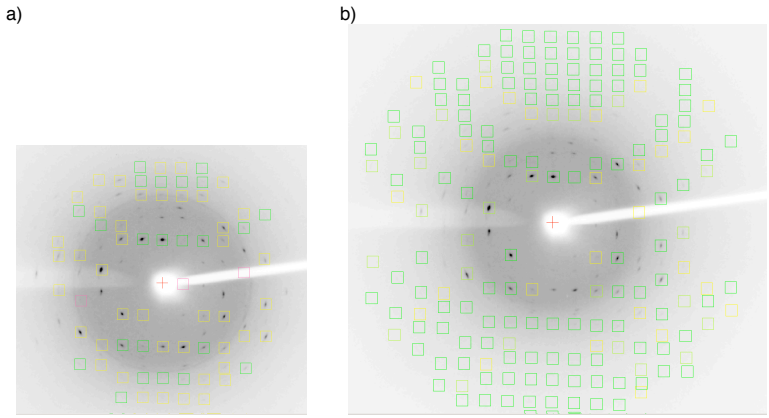

Figure S5. Diffraction patterns of a single-crystal fibre of **1** at 200 K (a) and 270 K (b).

Table S2. Experimental details of single crystal of **1** at 200 K.

Crystal data	
Crystal system, space group	Triclinic, *P*1
Temperature (K)	200
a, *b*, *c* (Å)	18.143(71), 26.330(105), 26.370(105)
α, β, γ (°)	89.045(25), 86.820(23), 86.714(23)
Radiation type	SR, λ = 0.701 Å
Crystal size (mm)	0.3×0.03×0.015
Data collection	
Diffractometer	SPring-8 BL02B1, CCD
Absorption correction	–
No. of measured, independent and observed [$I > 2\sigma(I)$] reflections	1187, 903, 112
R_{int}	31.72
$(\sin\theta/\lambda)_{max}$ (Å^{-1})	0.1666

Table S3. Experimental details of single crystal of **1** at 270 K.

Crystal data	
Crystal system, space group	Triclinic, *P*1
Temperature (K)	270
a, *b*, *c* (Å)	18.176(40), 26.391(59), 26.391(59)
α, β, γ (°)	89.0982(140), 86.9685(129), 86.6874(136)
Radiation type	SR, λ = 0.701 Å
Crystal size (mm)	0.3×0.03×0.015
Data collection	
Diffractometer	SPring-8 BL02B1, CCD
Absorption correction	–
No. of measured, independent and observed [$I > 2\sigma(I)$] reflections	5753, 968, 4919
R_{int}	23.56
$(\sin\theta/\lambda)_{max}$ (Å^{-1})	0.1666

SR powder XRD measurement and structure determination by a genetic algorithm (GA).

The SR diffraction experiments of the **1** powder sample with an imaging plate (IP) as the detector were carried out on the SPring-8 BL02B2 beam line. The wavelength of the incident X-rays was 0.8000(1) Å. The diffraction data were collected at 200 K. The exposure time of the measurement was 90 min. For temperature control, a N_2 gas flow system was used.

The crystal structure of **1** at 200 K was determined by the structure solution system based on a GA.[S3a] Information about the unit cell and space group from single-crystal diffraction was used in the analysis. The cell vectors ***a***, ***b***, ***c*** of the single-crystal unit cell were remerged to ***b***, ***c***, ***–a***. The total number of degrees of freedom of **1** was 27, including 3 orientation parameters and 24 torsion angles for one independent molecule. The hydrogen atoms were omitted from the structure model used in the GA analysis. The GA analysis was carried out using a program accelerated by the graphics processing unit (GPU).[S3b] The calculation speed of the GPU-accelerated program was approximately 100 times faster than that of a normal personal computer. For analysis, more than 100 billion trial structures are created and their powder patterns are simulated. Figure S4 shows the fitting result of the Rietveld refinement. The reliability factors of the final Rietveld refinement were Rwp = 5.8% and RI = 11% with d > 5.8 Å d-spacing range. The data resolution was insufficient for atomic-scale structure solution. The possible candidate of the structure model is shown in Figure 2a–c. The structure appeared to have quasi-1D pores towards the a-axis direction. The dimensions for crystallographic axis are 0.408, 0.138, and 0.733 for x, y, and z direction in the fractional coordinate.

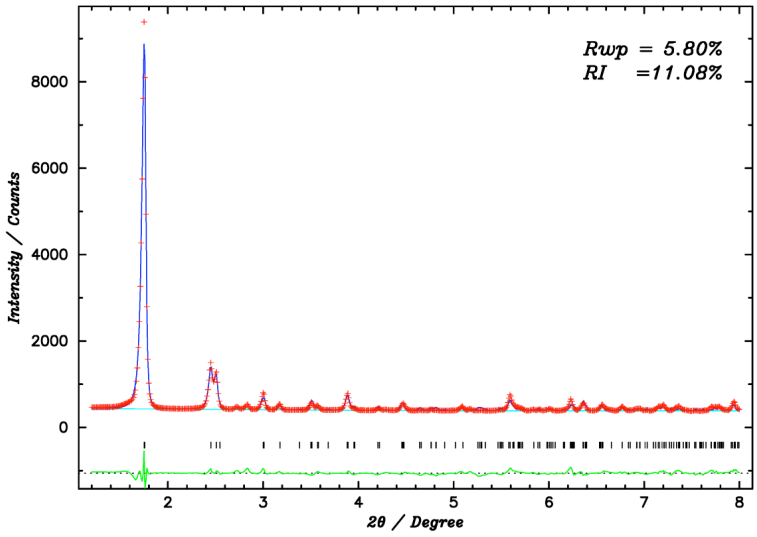

Figure S6. The Rietveld analysis of the SR-PXRD pattern of the fibres of **1** (λ = 0.701 Å).

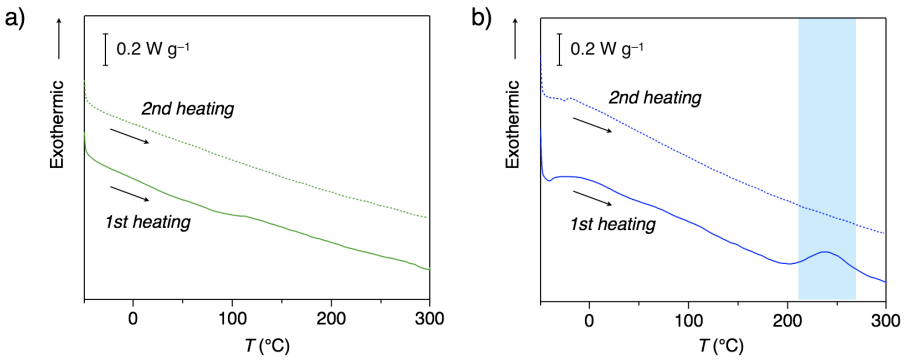

Figure S7. DSC traces on first (solid) and second (dotted) heating cycles of the self-assembled spheres (a) and fibres (b) of **1**.

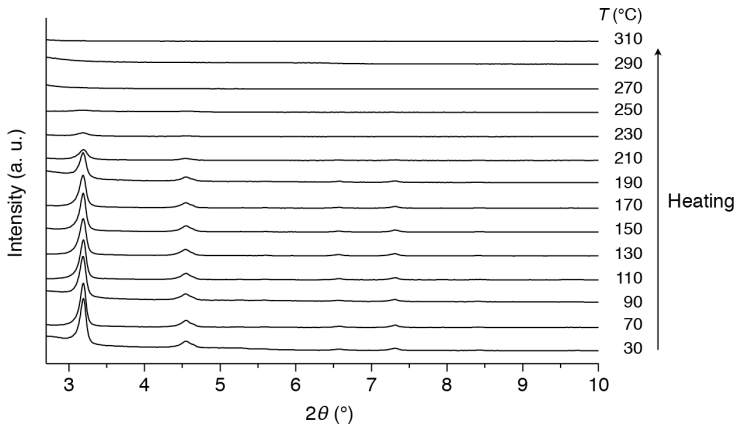

Figure S8. Temperature dependent powder XRD patterns of self-assembled fibres of **1** upon heating from 30 to 310 °C. Cu$K\alpha$ line with λ = 1.5405 Å was used for the X-ray source.

4. PL change upon solvent sorption.

PL spectra under acetonitrile and MeOH vapour were measured on Fluorolog-3 (HORIBA Jobin Yvon Inc.) with double-grating monochromators, 450-W xenon lamp, and R928 photomultiplier tube run in photon-counting mode.

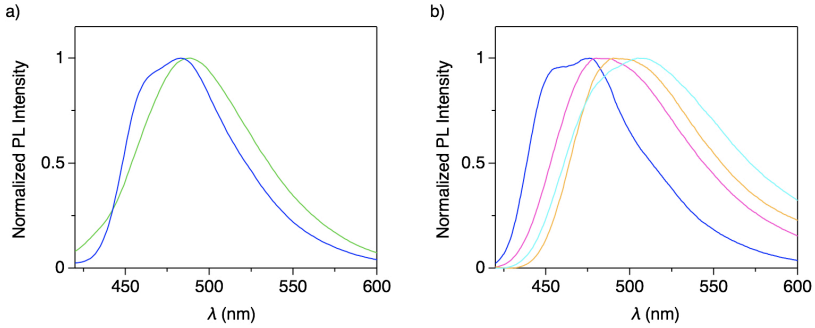

Figure S9. (a) PL spectra of cast films of self-assembled microfibres (blue) and microspheres (green) of **1** in air. CIE coordinates of the fibres and spheres are (0.152, 0.272) and (0.173, 0.337), respectively. (b) PL spectra of self-assembled fibres of **1** dispersed in hexane (blue), acetone (pink), acetonitrile (orange), and MeOH (light blue). PL of the fibres, dispersed in apolar hexane, displayed similar spectrum to that in air. As the polarity of the nonsolvent increased, i. e. fibres were dispersed in acetone, acetonitrile, and MeOH, the PL spectra showed clear red shift because the excited state is stabilized by the interaction with polar nonsolvents.[S3]

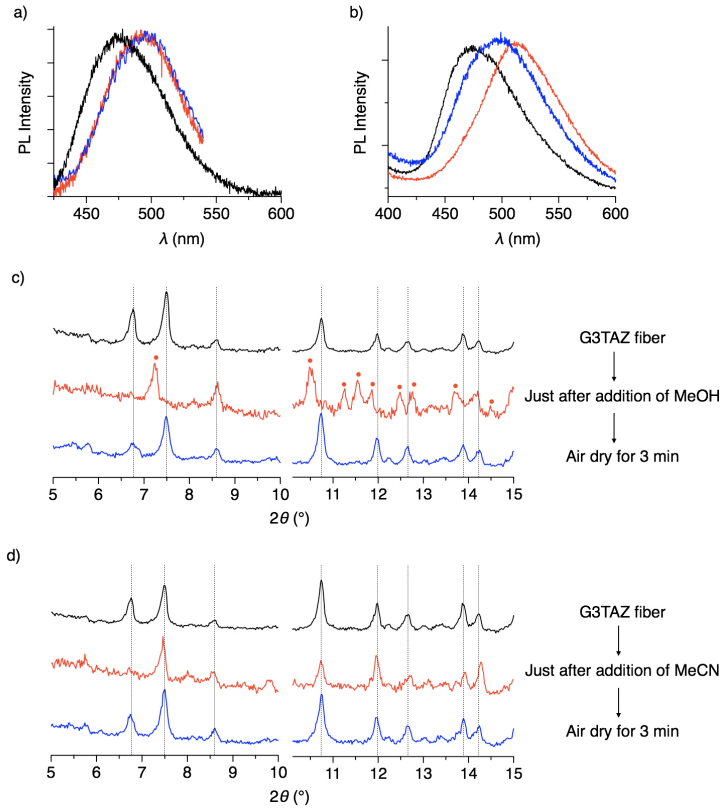

Figure S10. (a, b) PL spectra of the fibres of **1** upon introduction of acetonitrile (a) and MeOH (b) vapour. In (**A**), P/P_0 ~ 0 (black), 0.432 (red), and 0.982 (blue). In (b), P/P_0 = 0.092 (black), 0.460 (red), and 0.873 (blue). (c, d) Powder XRD patterns of the fibres of **1** with addition and evapouration of MeOH (c) and acetonitrile (d). Black, before addition; red, just after addition; blue, air dried for 3 min after addition.

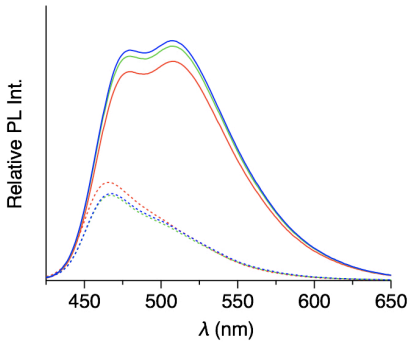

Figure S11. PL spectra of a cast film of microfibres of **1** in air (dotted) and in MeOH vapour (solid). Red, green, and blue curves indicate spectra on 1st, 2nd, and 3rd cycles.

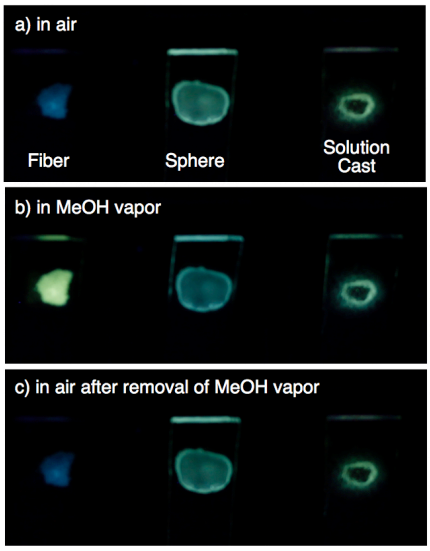

Figure S12. Fluorescent microscopy images of microfibres (left), microspheres (center), and a cast film from $CHCl_3$ solution of **1** in air (a), upon exposure to MeOH vapour (b), and in air after removal of MeOH vapour (c).

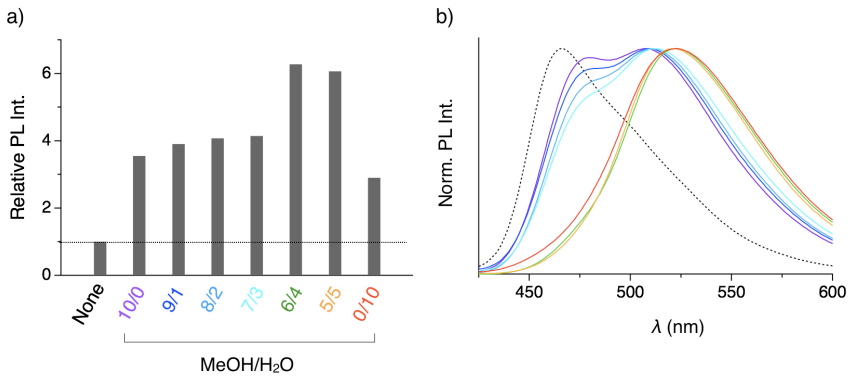

Figure S13. a) Bar graph of the PL area intensity of cast films of the porous microfibres of **1** in vapours of MeOH/H_2O cosolvents with different mixing ratio relative to that without vapour in air. b) Normalized PL spectra of cast films of the porous microfibres of **1** in air (dotted curve) and in vapours of MeOH/H_2O cosolvents (solid curves). The color of the spectra corresponds with the color of the description of the solvents in a).

5. Penetration of small π-conjugated molecules.

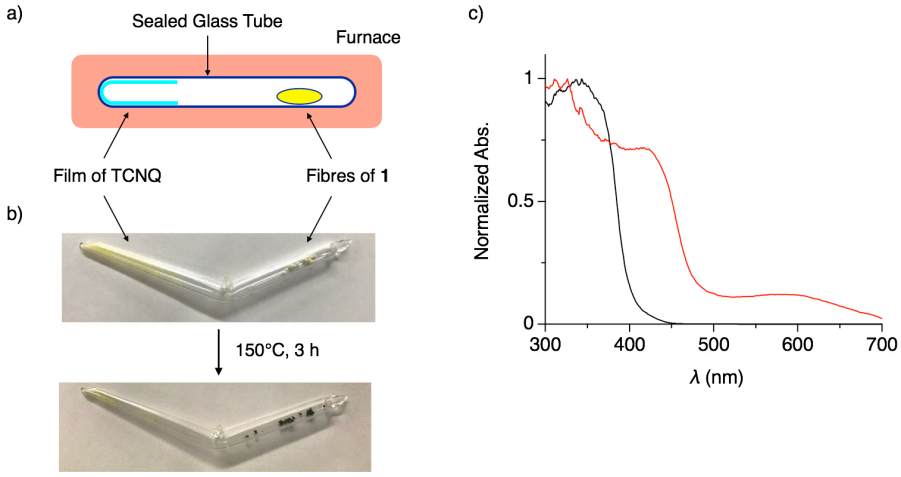

Figure S14. (a) Schematic representation of the annealing system for penetrating TCNQ into the microfibres of **1**. (b) Photographs of the sealed glass tube containing TCNQ (thin film, left side) and microfibres of **1** (powder, right side) before annealing (top) and after annealing for 3 h at 150 °C (bottom). (c) Photoabsorption spectra of microfibres of **1** (black) and those containing TCNQ (red). The powders of the samples were dispersed in polydimethylpolysiloxane (PDMS) matrix.

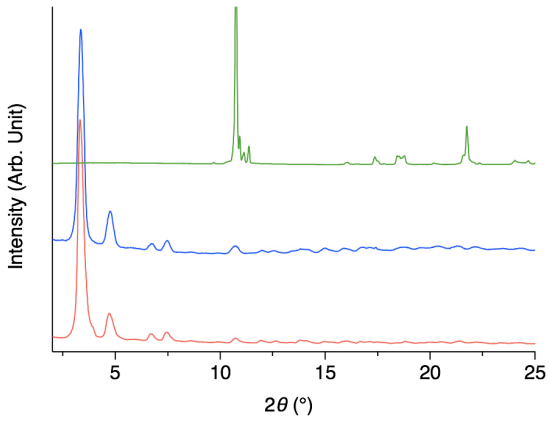

Figure S15. Powder XRD patterns of microfibres of **1** (red) and that after penetrating TCNQ (blue), along with that of TCNQ only (green).

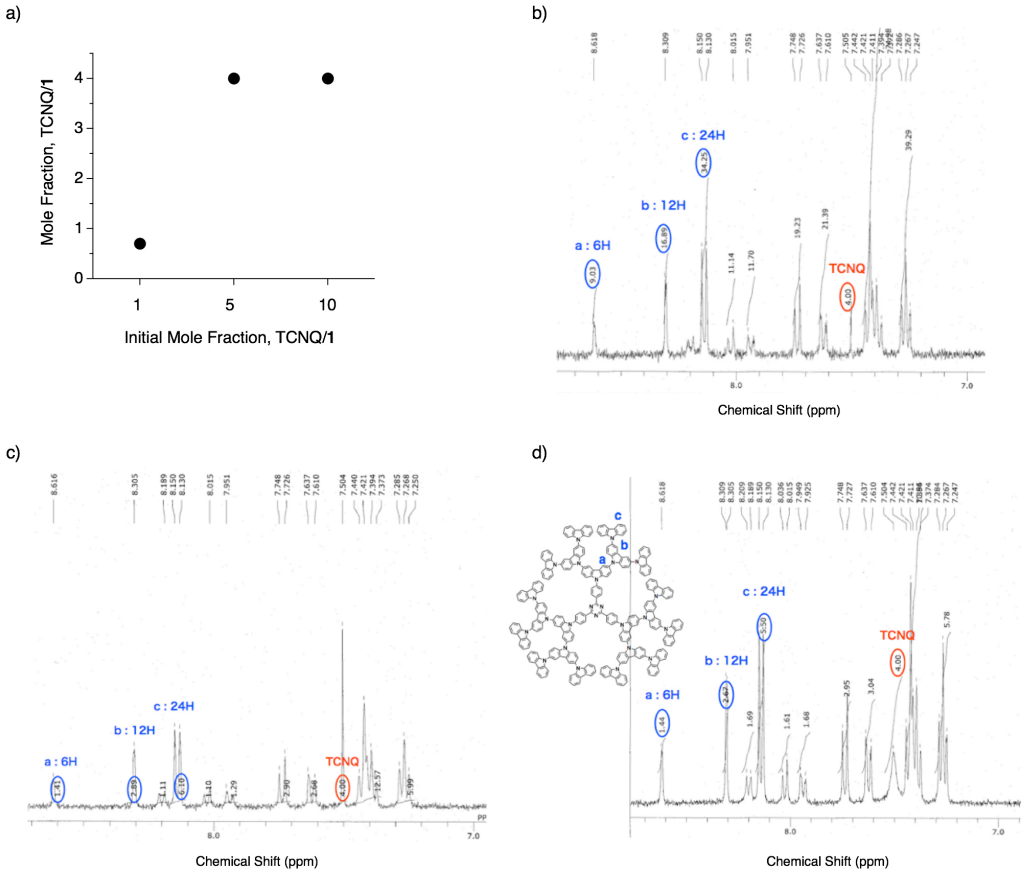

Figure S16. (a) Plot of the mole fraction TCNQ/**1** in the resultant microfibres of **1** after annealing in the sealed glass tube versus the initial mole fraction TCNQ/**1**. (b–d) ^{1}H-NMR chart of the dissolved microfibres of **1** penetrated with TCNQ. The molar ratios of **1** to TCNQ initially included in the glass tube are 1 : 1 (a), 1: 5 (b) , and 1 : 10 (c).

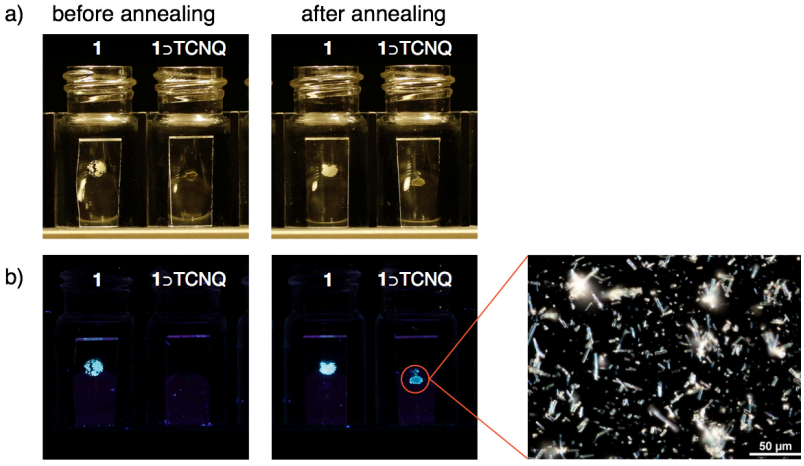

Figure S17. Optical photographs (a) and fluorescent photographs (b) of cast films of microfibres of **1** without (left) and with (right) penetration of TCNQ (left) before and after annealing at 150 °C in air.

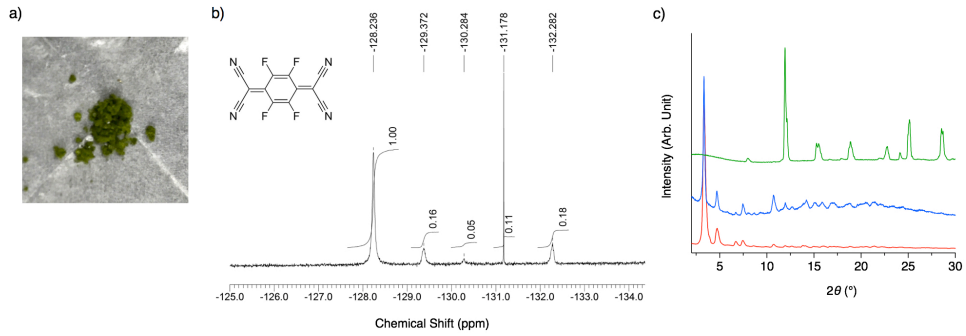

Figure S18. (a) Photograph of a powder of microfibres of **1** after penetration of F4-TCNQ. The sublimation condition: 150 °C, 3 h. (b) ^{19}F-NMR spectrum of **1**/F4-TCNQ composite, dissolved in $CDCl_3$. C_6F_6 was used as a standard. (c) Powder XRD patterns of microfibres of **1** (red) and that after penetrating F4-TCNQ (blue), along with that of F4TCNQ only (green).

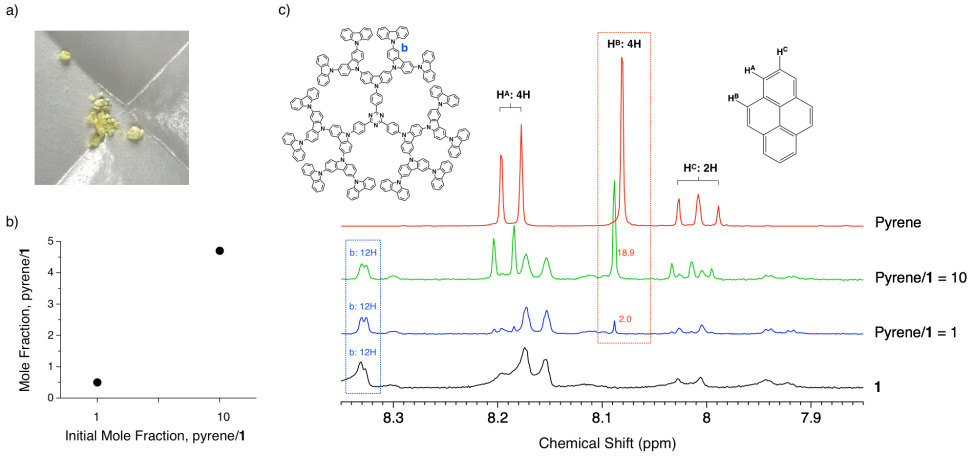

Figure S19. (a) Photograph of a powder of microfibres of **1** after penetration of pyrene. The sublimation condition: 130 °C, 1 h. (b) Plot of the mole fraction pyrene/**1** in the resultant microfibres of **1** after annealing in the sealed glass tube versus the initial mole fraction pyrene/**1**. (c) ^{1}H-NMR chart of the dissolved microfibres of **1** penetrated with pyrene, in addition of the charts of pyrene only (red) and **1** only (black) in $CDCl_3$. The molar ratios, pyrene/**1**, initially included in the glass tube, are 1 (blue) and 10 (green).

6. Supporting References

S1. K. Albrecht, K. Matsuoka, K. Fujita, K. Yamamoto, *Angew. Chem. Int. Ed*. **2015**, 54, 5677.

S2. a) K. D. M. Harris, M. Tremayne, P. Lightfoot, P. G. Bruce, *J. Am. Chem. Soc.* **1994**, *116*, 3543-3541. b) E. Nishibori, T. Ogura, S. Aoyagi, M. Sakata, *J. Appl. Cryst.* **2008**, *41*, 292-301.

S3. C. Reichardt, *Chem. Rev*. **1994**, *94*, 2319-2358.

S4. J. C. Nelson, J. G. Saven, J. S. Moore, P. G. Wolynes, *Science* **1997**, *277*, 1793-1796; R. B. Prince, J. G. Saven, P. G. Wolynes, J. S. Moore, *J. Am. Chem. Soc.* **1999**, *121*, 3114-3121; S. Kushida, O. Oki, H. Saito, J. Kuwabara, T. Kanbara, M. Tashiro, M. Katouda, Y. Imamura, Y. Yamamoto, *J. Phys. Chem. Lett.* **2017**, *8*, 4580-4586.